Journal of Solid State Chemistry **142,** 349–359 (1999)
Article ID jssc.1998.8043, available online at http://www.idealibrary.com on IDEAL®

Structural and Conductivity Properties of $Bi_{0.775}Ln_{0.225}O_{1.5}$ Oxide Conductors (Ln = La, Pr, Nd, Sm, Eu, Gd, Tb, Dy) with Rhombohedral Bi–Sr–O Type

M. Drache,[1] S. Obbade, J. P. Wignacourt, and P. Conflant

Laboratoire de Cristallochimie et Physicochimie du Solide, URA CNRS 452, USTL-ENSCL, BP 108, 59652 Villeneuve d'Ascq Cedex, France

Received June 1, 1998; in revised form September 22, 1998; accepted September 23, 1998

This paper deals with structural and conductivity properties of the dimorphic $Bi_{0.775}Ln_{0.225}O_{1.5}$ (Ln = La, Pr, Nd, Sm, Eu, Gd, Tb, Dy) hexagonal structure layer phases with rhombohedral Bi–Sr–O type. The evolutions, versus Ln^{3+}_{VI} radius, of cell parameters, thermal expansion coefficients, electrical properties (conductivity and activation energy), and structural characteristics determined from Rietveld powder structure refinements, suggest two different domains (La–Sm) and (Gd–Dy), with the intermediate Eu sample, thus possibly characterizing two kinds of ordering in the mixed cationic layer. The best conductivity properties obtained for $Bi_{0.775}La_{0.225}O_{1.5}$ ($\sigma_{400°C} = 10^{-3}$ S cm^{-1} with $E_a = 0.8$ eV) are discussed and justified. © 1999 Academic Press

INTRODUCTION

Numerous Bi_2O_3-based solid solutions with layered hexagonal structure are obtained by various cationic substitutions of M^{n+} for Bi^{3+} (M = alkaline earth (1–3), lanthanide or Y (4–7), alkaline earth + lead (8, 9)). These materials adopt a structural model, the so-called Bi–Sr–O rhombohedral structural type (10), based on the crystal structure of $Bi_{0.851}Sr_{0.149}O_{1.425}$. Since this first study, many single crystal investigations of the room temperature β_2 form have been realized by X-ray diffraction (3, 11–13) or by neutron diffraction (14); further studies of this phase have been done on powder samples either by neutron diffraction (14, 15) or by electron microscopy (16, 17).

The structure is built from cationic slabs parallel to (0 0 1) faces of the hexagonal cell, one slab being constituted from a mixed Bi^{3+}/M^{n+} layer sandwiched between two Bi^{3+} layers where two oxygen sites, $O_{(1)}$ and $O_{(2)}$, are located. The complementary oxide ions ($O_{(3)}$), implied by the formulation stoechiometries, are distributed over one or two sites of the interlayer space between slabs, and are characterized by partial occupancy factors. Depending on the system, a β_1 high temperature form with an hexagonal closely related structure is observed.

Both β_2 and β_1 phases exhibit a significant conductivity; it has been unambiguously attributed to an oxide ion moving inside the interlayer gap from anisotropic conductivity behavior measured out of a single crystal of $Bi_{0.851}Sr_{0.149}O_{1.425}$ (11).

A detailed investigation of corresponding bismuth–alkaline earth mixed oxides has shown that the $\beta_2 \rightarrow \beta_1$ phase transition occurs with an increase of log σ of about one unity accompanied by a weak and sudden enlargement of the cell parameters (11); it corresponds to the migration of the $O_{(2)}$ ions toward the interlayer space through specific pathway windows defined by three Bi neighboring atoms of the bismuth external layers of the slab. Particularly for the Bi_2O_3–SrO solid solution which has the more extended composition domain, the evolutions versus composition of characteristics such as the $\beta_2 \rightarrow \beta_1$ transition temperature and enthalpy, isothermal conductivities and activation energies of β_2, and c cell parameter expansion during $\beta_2 \rightarrow \beta_1$ transition exhibit maxima or minima values. These extrema have been linked to the existence of one (M = Ca, Ba) or two (M = Sr) kinds of ordering of Bi and alkaline earth cations in the mixed layer for the β_2 low temperature form, thus leading to a superstructure. Each supercell, which is triclinic, results from a combination of parameters of the subcell (17). The cationic order in the mixed layer cannot exist over the $\beta_2 \rightarrow \beta_1$ transition temperature and disappears, leading to the sudden increase of the a lattice parameter (and therefore of the $O_{(2)}$ pathway window). The increase of the number of oxide ions in the intersheet space is accompanied by an enlargement of the c parameter and conductivity level.

A systematic investigation of specific compositions $Bi_{0.775}Ln_{0.225}O_{1.5}$ (Ln = La, Pr, Nd, Sm, Eu, Gd, Tb, Dy) selected as the reference, has been made in order to check the rhombohedral polymorphism (7). Different types of evolutions, depending on the Ln nature, are obtained upon heating of the β_2 low temperature form: one leads to the

[1]To whom correspondence should be addressed. Fax: (33)320436814. E-mail: drache@ensc-lille.fr.

0022-4596/99 $30.00

closely related β_1 high temperature form for Ln = La–Sm (β_1 + fcc δ-Bi_2O_3-related phase mixture for Ln = Eu, Gd) and further to a fcc δ-Bi_2O_3-related phase for Ln = Sm–Gd; another goes directly to this fcc structural type (Ln = Tb–Er); in this case the $\beta_2 \rightarrow \delta$ transformation appears irreversible under dynamic cooling conditions (cooling rate $\geq 5°C\ min^{-1}$).

The crystal structure investigation of $Bi_{0.7}La_{0.3}O_{1.5}$ powder sample (13), using X-ray or neutron diffraction, did not reveal any cationic order in the mixed layer; however, for this mixed oxide and also for $Bi_{0.775}Ln_{0.225}O_{1.5}$ (Ln = La, Pr, Nd, Sm, Eu, Gd) the β_2/β_1 polymorphism makes it possible to reasonably presume the existence of a cation and/or anion order in the mixed layer of the β_2 phase, which disappears during the $\beta_2 \rightarrow \beta_1$ transition.

This paper describes structural and conductimetry investigations of $Bi_{0.775}Ln_{0.225}O_{1.5}$ hexagonal phases in order to build correlations between structure–conductivity properties and to complete the knowledge of these phases.

EXPERIMENTAL

$Bi_{0.775}Ln_{0.225}O_{1.5}$ powder samples have been prepared by solid state reaction of Bi_2O_3 and Ln_2O_3 oxides (purities of 99.9%). The reactants were prefired for dehydration at 600–700°C in air before use. Stoichiometric proportions were accurately weighted and intimately ground in an agate mortar. Each mixture was transferred into an alumina crucible and heated at 650°C for two 15-h treatments; each thermal treatment was followed by a regrinding. The end of the synthesis characterized by the purity of the hexagonal phase at room temperature, was checked by X-ray diffractometry using a Guinier de Wolff camera (Cu$K\alpha$ radiation).

The thermal behavior of all samples has been investigated by two techniques:

- X-ray thermodiffractometry studies were carried out using a Siemens D5000 X-ray diffractometer equipped with a Siemens HTK10 high-temperature device (heating platinum plate; average heating rate, $300°C\ h^{-1}$; air gas flow). In order to prevent any reaction between platinum sample holder and the investigated materials, the samples were deposited on a gold plate using an ethanol slurry which yields upon evaporation a regular layer of powdered compound.
- Conductivity measurements were made on samples pelletized at room temperature (diameter 5 mm, thickness ca. 3 mm) and then sintered at 900°C for 2 h and annealed at 600°C for 60 h. The degree of compaction in all cases ranged between 75 and 92%. Gold electrodes were vacuum deposited on both flat surfaces of pellets using the sputtering method. The measurements were obtained by impedance spectrometry in the frequency range 1–10^6 Hz, using a Schlumberger 1170 frequency response analyzer; for a given temperature, each set of values was recorded after a 1 h stabilization time.

Room temperature structures of $Bi_{0.775}Ln_{0.225}O_{1.5}$ samples have been investigated using the Rietveld method.

Powder diffraction data were recorded on a Siemens D5000 diffractometer using a Bragg–Brentano geometry with a back monochromatized Cu$K\alpha$ radiation. Diffraction patterns were scanned by steps of 0.03° (2θ) over the angle range 10–120°, with a counting time of 50 s per step. In order to minimize the orientation effects that occur when powdered samples are pressed, for each material a side loading method was used and the sample was rotated at 3.14 rad s^{-1} during the data recording. The precise positions of the peaks were evaluated by means of the fitting program FIT available in the PC software package DIFFRAC-AT from SOCABIM.

The structure refinement was carried out with the Rietveld profile refinement technique (18, 19) by means of the program FULLPROF (20) based on version DbW3.2S (8804) of the Rietveld code published by R. A. Young and D. B. Wiles (21). The peak shape was represented by a pseudo-Voigt function with an asymmetry correction at low angles. In order to describe the angular dependence of the peak full-width at half-maximum (H), the formulation of Caglioti *et al.* (22) was used: $H^2 = U \tan^2\theta + V \tan\theta + W$, where U, V, and W parameters were refined in the process. The background was represented by a polynomial of degree 5 in 2θ. The procedure involved the refinement of other parameters (scale factor, effective 2θ zero of the instrument, atomic coordinates, cell parameters, and thermal parameters). At the end of the refinement, the good matching between observed and calculated data was indicated by the significant values of the profile reliability factors (R_p, R_{wp}) and the crystal structure model quality factors (R_F, R_{Bragg}).

RESULTS

The accurate cell parameters of the $Bi_{0.775}Ln_{0.225}O_{1.5}$ materials have been refined from 111 independent reflections on the basis of hexagonal cells from precise peak positions determined under the typical conditions described under Experimental. The results, in good agreement with the previously published refined cell parameters (7), are reported versus Ln^{3+} radius (24, 25) (Fig. 1).

Two kinds of linear variations of cell parameters versus lanthanide radius are observed: one for Ln = La, Pr, Nd, Sm, Eu and another one for Ln = Gd, Tb, Dy. The weak differences between these behaviors can justify that only one type of linear dependence of cell volume was previously presented (7).

X-ray thermodiffractometry has been used to observe the high temperature modifications of both series on a D5000 diffractometer, during a heating run between room temperature and 900°C. The X-ray reflections were indexed in

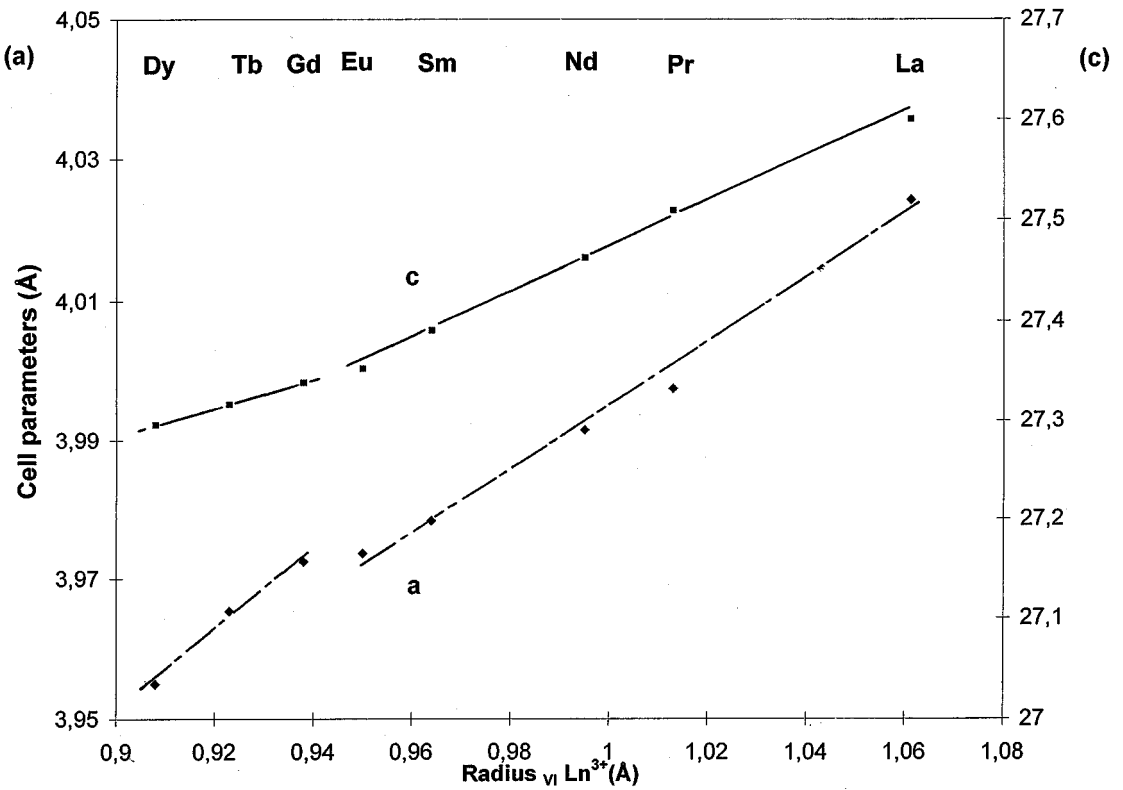

FIG. 1. Evolution of $Bi_{0.775}Ln_{0.225}O_{1.5}$ room temperature lattice constants versus Ln^{3+} $radius_{VI}$.

hexagonal cells with the rhombohedral symmetry of the Bi–Sr–O-type phases ($a \cong 4$ Å, $c \cong 28$ Å); the cell parameters were refined for the different investigated temperatures (step scan: 100°C from 100 to 600°C and 50°C from 650 to 900°C).

For all samples, a pseudolinear domain is typical of the evolutions of the lattice constants a and c versus the temperature between 20 and 700°C. Over this temperature range, for Ln = La, Pr, Nd, Sm, and Eu, a sudden increase of both parameters characterizes the $\beta_2 \rightarrow \beta_1$ transition, which occurs between 700 and 750°C for Ln = La; again, linear domains of temperature–cell parameters dependences are obtained for the β_1 high temperature form (Fig. 2). From La to Eu lanthanide, the observed temperature of the phase transition increases; as a result from the maximum temperature of investigation (900°C), the cell parameters versus temperature domains related to β_1 become narrow, and this is characterized only by one cell parameters refinement for $Bi_{0.775}Eu_{0.225}O_{1.5}$ with the standard recording conditions. For Ln = Gd, Tb, and Dy, the formation of an fcc phase occurs between 700 and 900°C and is preserved at room temperature when the sample is quenched; this is in a fairly good agreement with the previous thermal investigation of these materials using a Guinier-Lennè camera (7). In this previous study, the absence of β_1 formation with Ln = Pr and Nd and the reversibility of the transformation for Ln = Gd was signaled. The slight disagreement with the present work is likely to be attributed to the big difference between the chosen heating speeds (20°C h^{-1} for Guinier-Lennè camera—300°C h^{-1} as averaged heating rate for Siemens D5000 X-ray diffractometer). The formation of an fcc δ-type phase, which results from a progressive displacement of the composition domains of the hexagonal phases (Ln = Pr and Nd) when the temperature increases, does not occur under high heating rates.

The cell parameters thermal expansion coefficients of the room temperature stable phase have been determined from the slopes of lattice constant versus temperature pseudolinear domains, for all samples, and are reported versus the Ln^{3+}_{VI} radius in Fig. 3. Particularly for c parameters, two types of linear dependences are observed: one for Ln = La, Pr, Nd, Sm, Eu and a second one for Ln = Gd, Tb, Dy.

The thermal investigation of conductivity properties of all materials $Bi_{0.775}Ln_{0.225}O_{1.5}$ has been realized during two successive treatment cycles (300–600 and 300–800°C). The results were interpreted from $\log \sigma = f(10^3/T)$ Arrhenius plots. For every sample, a pseudolinear domain was observed between 300 and 700°C, and after a fast jump of conductivity, a more or less similar domain shortly exists up to 800°C. These domains were identified on the basis of X-ray diffraction investigations of powder samples versus temperature and confirmed by the patterns of the materials

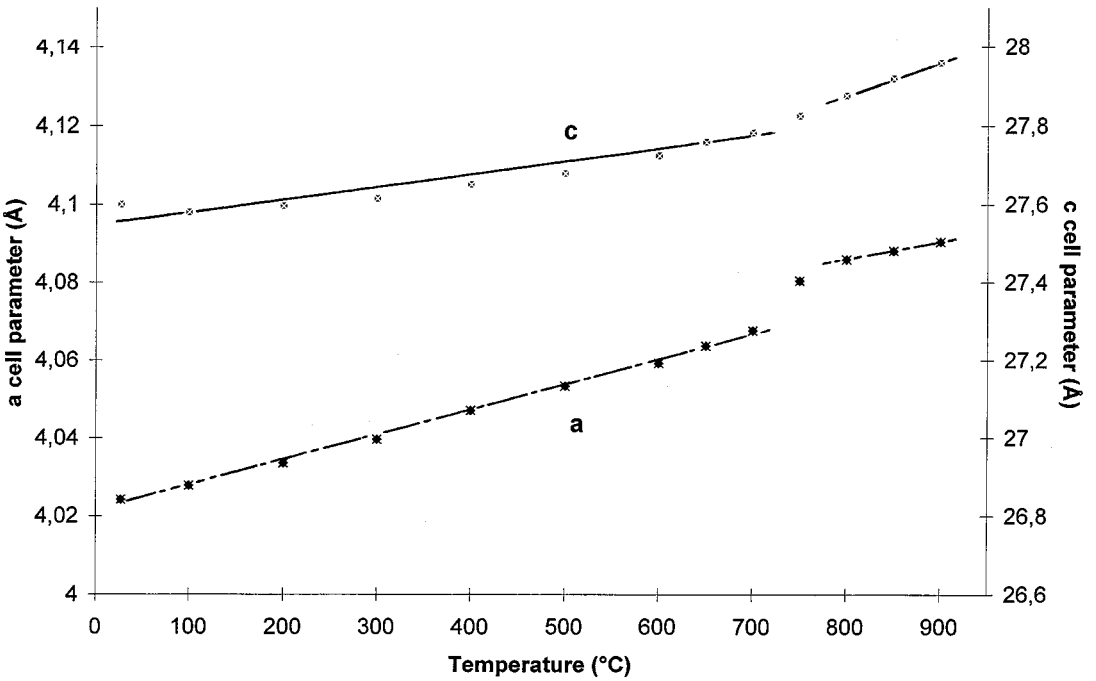

FIG. 2. Evolution of $Bi_{0.775}La_{0.225}O_{1.5}$ lattice constants versus temperature.

collected at the end of the measurements cycles on reground pellets. Figure 4 presents the plots corresponding to the second heating for Ln = La and Dy, respectively the largest and the smallest investigated lanthanide.

For Ln = La, two domains characterize the β_2 low-temperature form and then the β_1 high-temperature variety; the phase transition, perfectly reversible, leads upon cooling to reproducible conductivity values for each temperature.

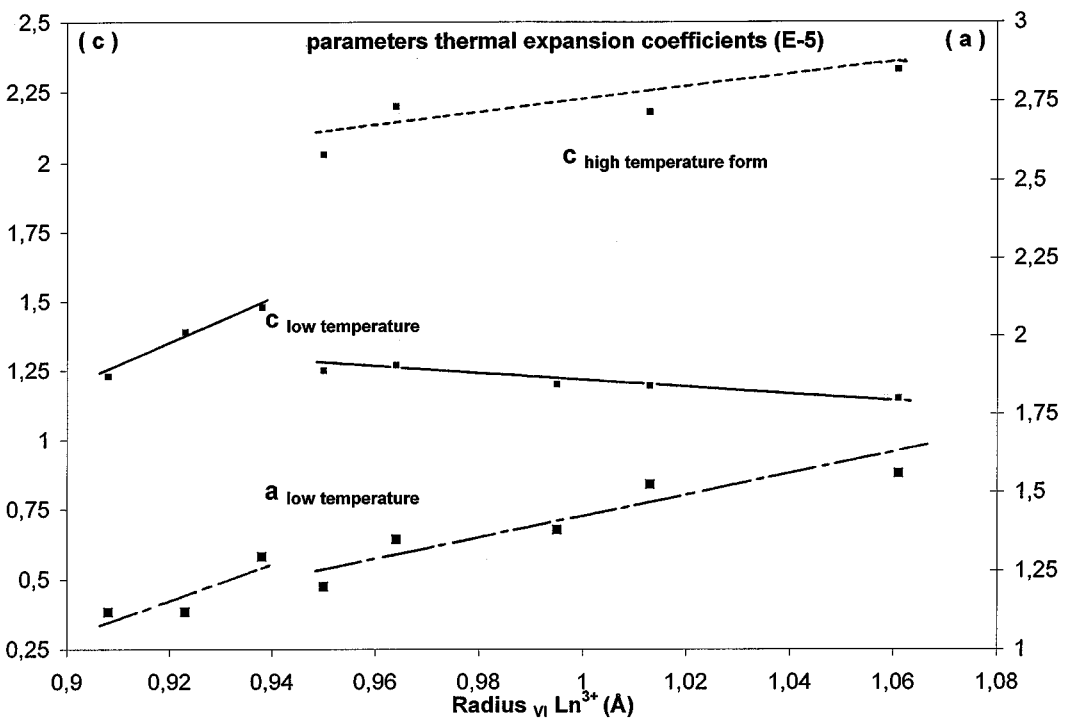

FIG. 3. Evolution of $Bi_{0.775}Ln_{0.225}O_{1.5}$ cell parameters thermal expansion coefficients versus Ln^{3+}_{VI} radius.

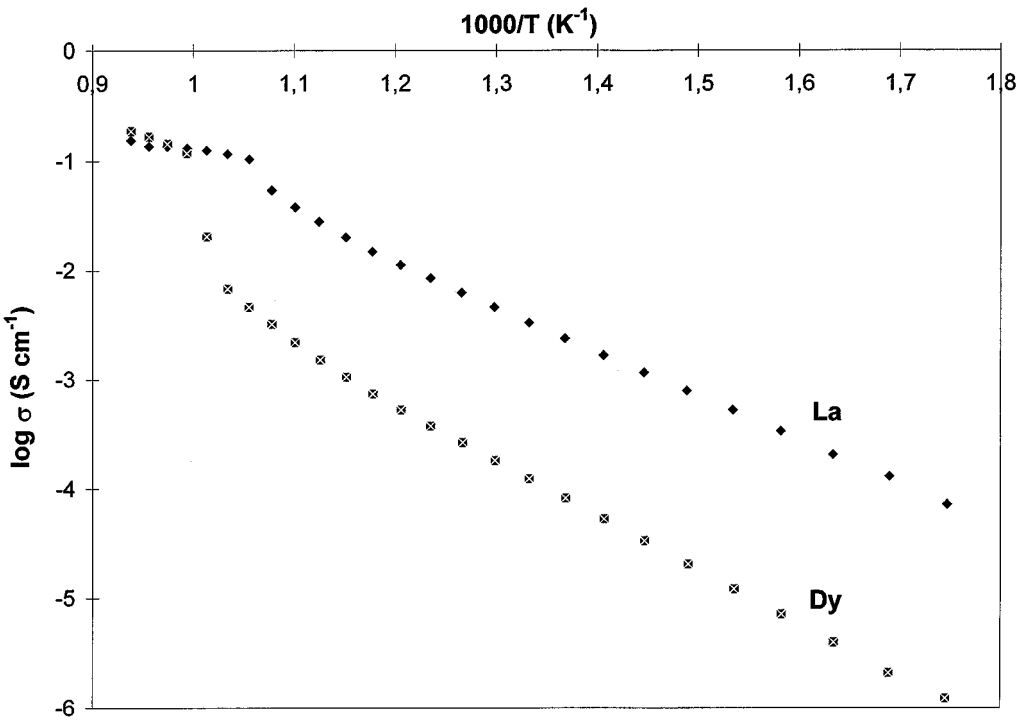

FIG. 4. Arrhenius plots for $Bi_{0.775}La_{0.225}O_{1.5}$ and $Bi_{0.775}Dy_{0.225}O_{1.5}$ (second heating).

For $Ln = Dy$, these domains correspond to the hexagonal room temperature stable phase and then to the fcc δ-type phase. This last one is partly preserved at low temperature during the cooling process, leading to nonreproducible σ values (σ heating $< \sigma$ cooling). Figure 5 shows the evolutions of the activation energies (Fig. 5a) and isothermal conductivities (Fig. 5b), measured at 400°C during the first cooling, versus the ionic radius of Ln^{3+} ions. As we have already noticed for the lattice constants and for the cell parameters thermal expansion coefficients, the electrical properties also present a specific behavior for Gd–Tb—Dy samples that is different from that of the other studied lanthanides.

The crystal structure refinements of $Bi_{0.775}Ln_{0.225}O_{1.5}$ materials have been conducted on the basis of the structural investigations of the $R\bar{3}m$ rhombohedral Bi–Sr–O–type phases (10, 12–14) in hexagonal cells ($Z = 9$) with the lattice parameters reported in Fig. 1 and in Table 1. The structures were refined considering a full Bi occupancy of 6*c* sites $(0, 0, z)$ and a statistical distribution of Bi and *Ln* atoms over 3*a* sites $(0, 0, 0)$, with occupancy coefficients fixed to fit the nominal compositions. The oxide ions were distributed over three sets of 6*c* sites as previously defined $O_{(1)}$, $O_{(2)}$, and $O_{(3)}$ (13). The refinements concerning the cations were realized on atomic coordinates of Bi (6*c* sites) and on anisotropic thermal parameters (all cations). For each oxide anion, refinements were done on atomic coordinates and on isotropic thermal parameters; the occupancy factors of $O_{(2)}$ and $O_{(3)}$ were correlated to fit the formulation and a common value for their isotropic thermal parameter was refined. Each refinement process was realized from 222 observed reflections with 29 fitted parameters. At the end of the refinement process, the agreement between observed and calculated data was indicated by the reliability factors R_{Bragg}, R_F, R_p, R_{wp} (Table 2) and by the plot of observed and calculated patterns for all $Bi_{0.775}Ln_{0.225}O_{1.5}$ investigated materials (Fig. 6). Table 3 summarizes the structural characteristics: To withdraw fractional coordinates along the *c* axis of Bi and O atoms (6*c* sites), $O_{(2)}$ and $O_{(3)}$ occupancy factors. Selected interatomic distances and thermal parameters are reported in Tables 4 and 5, respectively. Figure 7 gives a schematic representation of the structures. The evolutions of cationic slab thickness and interslab gap size versus the Ln_{VI}^{3+} ion radius are presented in Fig. 8.

DISCUSSION

The existence of two types of relationships observed for the evolutions of the cell parameters, the lattice constants thermal expansion coefficients, the electrical properties (activation energies and isothermal conductivities), and structural characteristics (cationic slab thickness and interslab distances) versus Ln_{VI}^{3+} radius, typical of the low temperature stable phases, can be interpreted as characterizing two types of Bi/*Ln* order in the mixed cationic layer. This suggests that it should be considered as previously done on

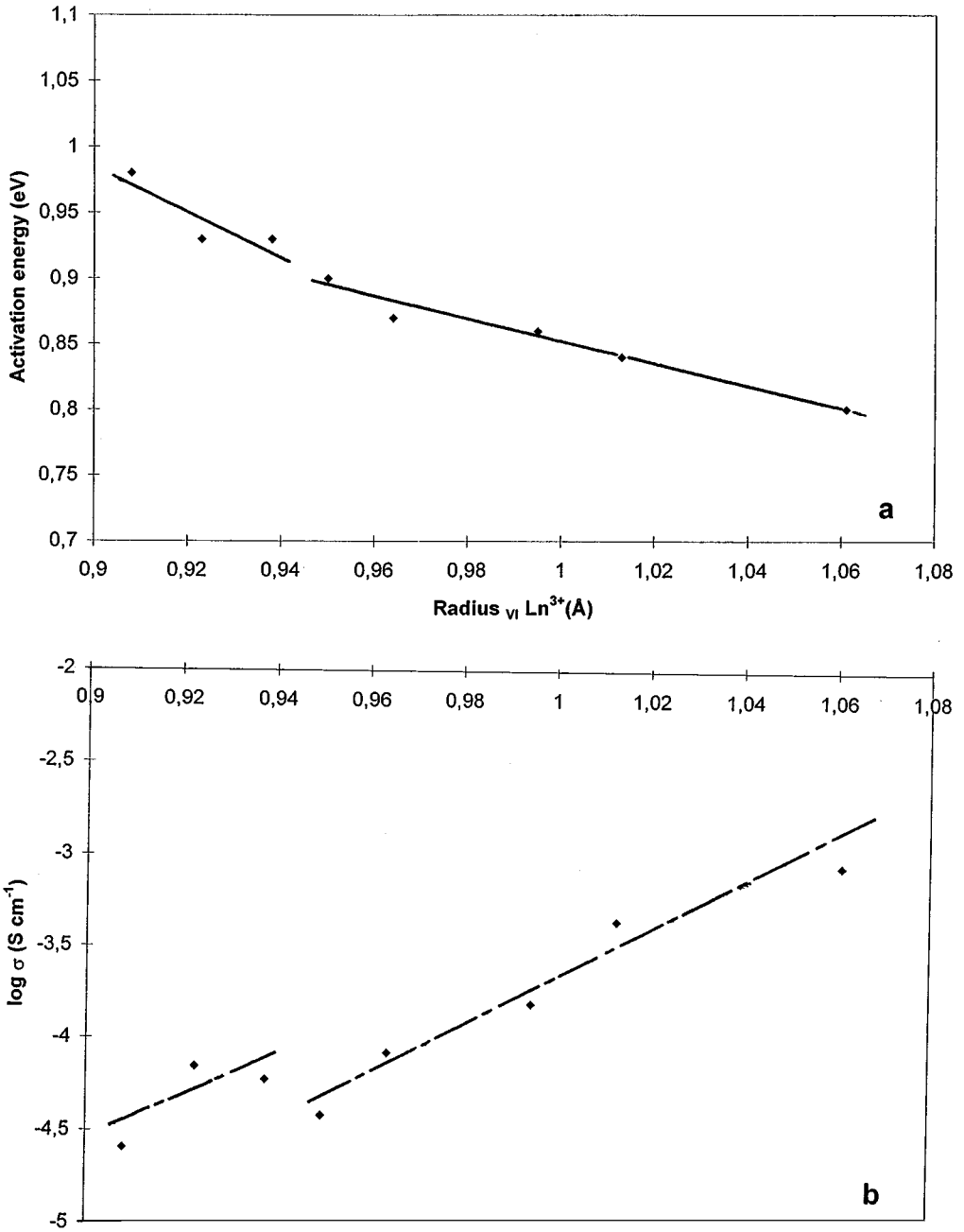

FIG. 5. Evolution versus Ln^{3+}_{VI} radius of activation energy (a) and isothermal (400°C) conductivity ($\log \sigma/\Omega^{-1}\,\mathrm{cm}^{-1}$) (b) for $Bi_{0.775}Ln_{0.225}O_{1.5}$.

the basis of the unit cell volume evolution (7), that all these phases exhibit the β_2 structural type. The two different observed evolutions could also correspond to a first set of β_2-type samples (Ln = La, Pr, Nd, Sm, Eu) and a second set of β_1 type in which the cations of the mixed layer are disordered; this would be in agreement with the absence of $\beta_2 \rightarrow \beta_1$ transition, particularly for Ln = Tb and Dy (7).

A comparison of the evolution of cell parameters thermal expansion coefficients of the pure β_1 high temperature variety for Ln = La, Nd, Sm, and Eu samples versus Ln^{3+} $\mathrm{radius_{VI}}$, using 25°C step scan in the 700–925°C range, with the similar evolution of the low temperature form of Ln = Gd, Tb, Dy samples has been done in order to check the possible identification of one single domain characterizing the β_1 type for this second set. An accurate determination of the β_1 cell parameters thermal expansion coefficients is not possible, due to the limited temperature range of stability for these samples. However, from estimated values

TABLE 1
$Bi_{0.775}Ln_{0.225}O_{1.5}$ Lattice Constants

Ln	*a* (Å)	*c* (Å)
La	4.0242 (2)	27.600 (1)
Pr	3.9975 (1)	27.509 (1)
Nd	3.9915 (1)	27.463 (1)
Sm	3.9783 (2)	27.391 (2)
Eu	3.9736 (2)	27.353 (2)
Gd	3.9724 (3)	27.339 (1)
Tb	3.9653 (2)	27.317 (2)
Dy	3.9549 (2)	27.296 (1)

of the *c* parameter corresponding coefficients, two domains can be drawn. Moreover, for $Ln = La$ and Pr samples, activation energies of β_1 (0.3 to 0.4 eV) and estimated $\log \sigma_{400°C}$ values (-1.5 to -1.7) ($\sigma/\Omega^{-1}\,cm^{-1}$), characteristic of this disordered variety, are respectively lower and higher than those estimated from $Ln = Gd$–Tb–Dy domains of Figs. 6a and 6b. From these considerations it is likely that both series of samples exhibit the β_2 structural type, with a cationic order in the Bi(1), *Ln* mixed layer for the first set being different of the order in the second one.

The results of the crystal structure investigations have been examined on the basis of the former assumptions. Table 3 evidences a decrease of the occupancy factors of $O_{(2)}$ ions in a first set from La to Sm, and then in a second one from Eu to Dy; in each set, $O_{(3)}$ occupancy factors, which are correlated to the $O_{(2)}$ factors, exhibit an increase. These evolutions can be related to the decrease of the Ln^{3+} ion size which implies smaller $O_{(2)}$ ions sites sizes and slab thickness. The existence of two types of cationic Bi/*Ln* order in a superstructure is not surprising, considering also that two types of supercell were found for β_2 in the Bi–Sr–O solid solution (11).

The interslab thickness is determined by the equilibrium of the repulsion effect between two neighboring slabs, which varies as a function of (slab thickness)$^{-1}$, and the attraction

TABLE 3
Characteristic Atomic Coordinates and Occupancy Factors for $Bi_{0.775}Ln_{0.225}O_{1.5}$

Ln	*z* $Bi_{(2)}$	*z* $O_{(1)}$	*z* $O_{(2)}$	*z* $O_{(3)}$	Occup. factor $O_{(2)}$	Occup. factor $O_{(3)}$
La	0.2243(1)	0.300(1)	0.092(1)	0.441(2)	0.82(2)	0.43(2)
Pr	0.2244(1)	0.302(1)	0.095(1)	0.445(2)	0.81(3)	0.44(3)
Nd	0.2247(1)	0.303(1)	0.097(1)	0.445(2)	0.77(3)	0.48(3)
Sm	0.2248(1)	0.305(2)	0.093(2)	0.445(2)	0.70(4)	0.55(4)
Eu	0.2253(1)	0.300(1)	0.090(1)	0.450(2)	0.81(2)	0.44(2)
Gd	0.2252(1)	0.299(1)	0.091(1)	0.446(1)	0.78(2)	0.47(2)
Tb	0.2252(1)	0.303(1)	0.088(1)	0.447(2)	0.78(2)	0.47(2)
Dy	0.2252(1)	0.300(1)	0.091(2)	0.452(2)	0.72(3)	0.53(3)

Note. 3*a* sites $Bi_{(1)}Ln(0, 0, 0)$ are statistically occupied by 0.975Bi and 2.025*Ln*; 6*c* sites $Bi_{(2)}$ and $O_{(1)}(0, 0, z)$ are fully occupied; occupancy factors of 6*c* sites $O_{(2)}$ and $O_{(3)}(0, 0, z)$ are correlated to fit the nominal composition.

effect between $O_{(3)}$ ions of the interslab gaps and the slabs themselves; the second effect varies as a function of $O_{(3)}$ sites occupancy factor. The slab thickness variation for the first set (from La to Sm) is large and therefore the variation of the repulsive effect is predominant and implies an interslab gap enlargement. For the second set (Eu to Dy) the variation of the slab thickness is negligible and the increase of $O_{(3)}$ ions number leads to a contraction of the interslab distance. Considering that, from Sm to Dy material, the slab thickness decreases, resulting mainly from the Ln^{3+} radius variation, the existence of two cationic order in the mixed layer implies an increase of the $O_{(2)}$ site size during the transition first set → second set; the sudden increase of the occupancy factor of these ions sites from Sm to Gd sample proves the validity of this hypothesis.

The $O_{(3)}$ ions mobility is directly depending on the bonds between these ions and the adjacent slabs and is therefore related to the charge density of cations within the slabs; the thinner the slabs, the stronger the charge density, and therefore the bonds. This is in good agreement with the regular

TABLE 2
Reliability Factors for $Bi_{0.775}Ln_{0.225}O_{1.5}$ Rietveld Structure Refinements

Ln	R_{bragg}	R_F	R_p	R_{wp}
La	0.060	0.059	0.104	0.147
Pr	0.094	0.069	0.114	0.149
Nd	0.074	0.069	0.109	0.148
Sm	0.099	0.084	0.145	0.199
Eu	0.062	0.060	0.118	0.156
Gd	0.067	0.064	0.085	0.116
Tb	0.062	0.060	0.101	0.138
Dy	0.095	0.071	0.122	0.174

TABLE 4
Selected Interatomic Distances for $Bi_{0.775}Ln_{0.225}O_{1.5}$

Ln	($Bi_{(1)}$, *Ln*)–$O_{(1)}$	($Bi_{(1)}$, *Ln*)–$O_{(2)}$	$Bi_{(2)}$–$O_{(1)}$	$Bi_{(2)}$–$O_{(2)}$
La	2.49 (1)	2.55 (2)	2.11 (2)	2.37 (1)
Pr	2.46 (1)	2.62 (3)	2.13 (3)	2.34 (1)
Nd	2.45 (1)	2.65 (3)	2.15 (3)	2.33 (1)
Sm	2.43 (1)	2.55 (4)	2.19 (3)	2.34 (1)
Eu	2.47 (1)	2.45 (3)	2.05 (3)	2.35 (1)
Gd	2.47 (1)	2.48 (2)	2.02 (2)	2.34 (1)
Tb	2.44 (1)	2.41 (3)	2.12 (3)	2.35 (1)
Dy	2.45 (1)	2.47 (4)	2.05 (3)	2.33 (1)

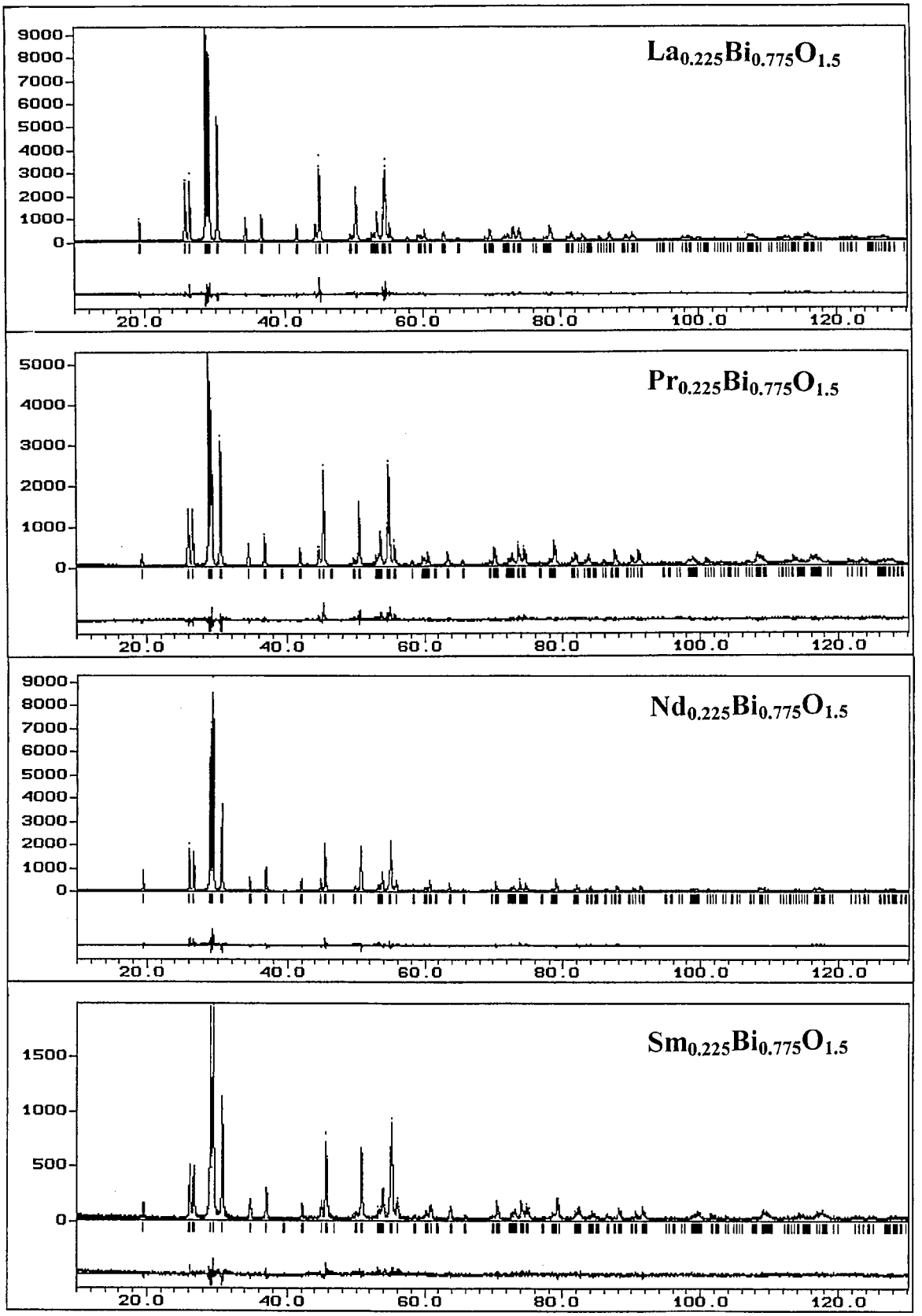

FIG. 6. Observed and calculated patterns for $Bi_{0.775}Ln_{0.225}O_{1.5}$.

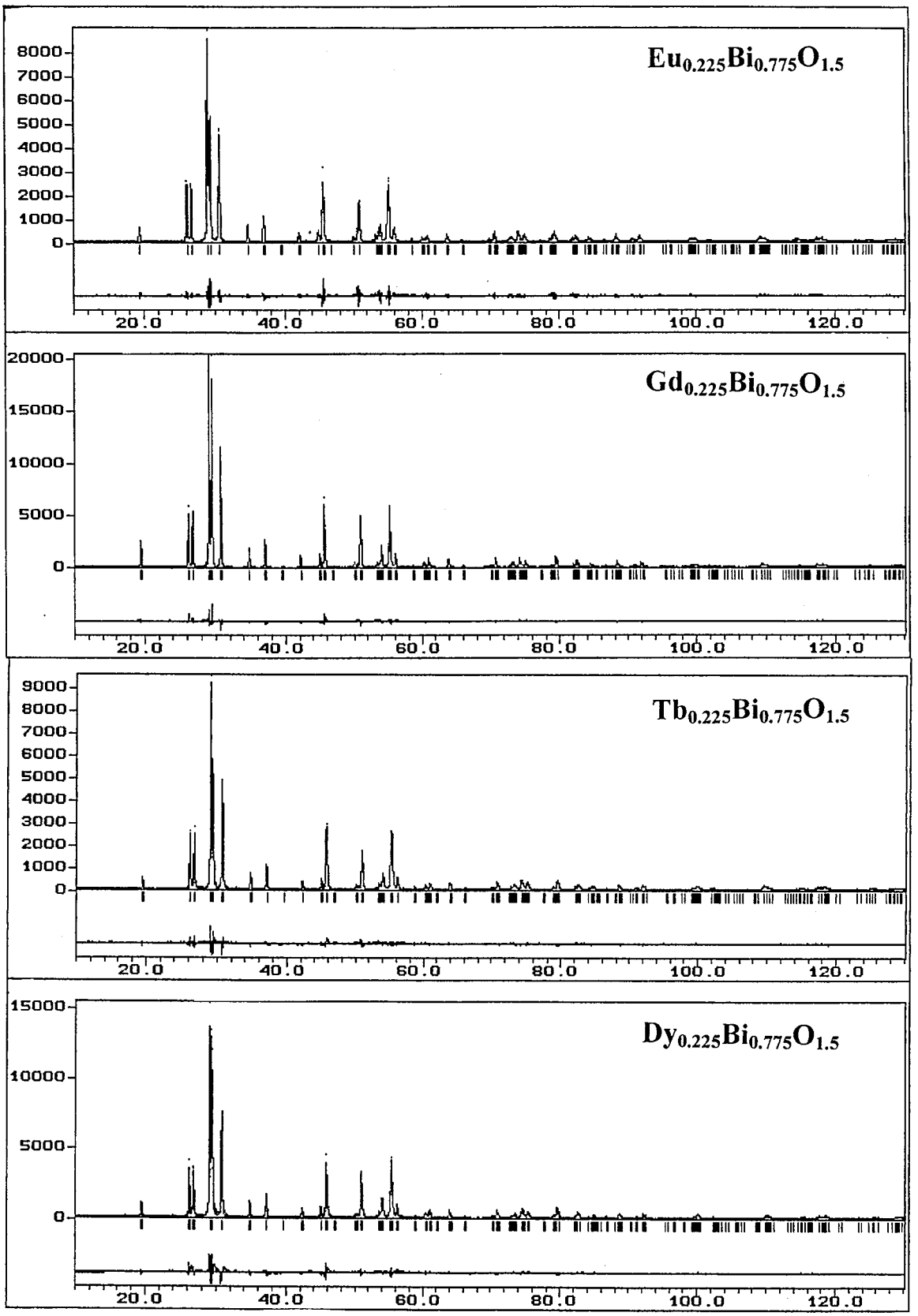

FIG. 6—*Continued*

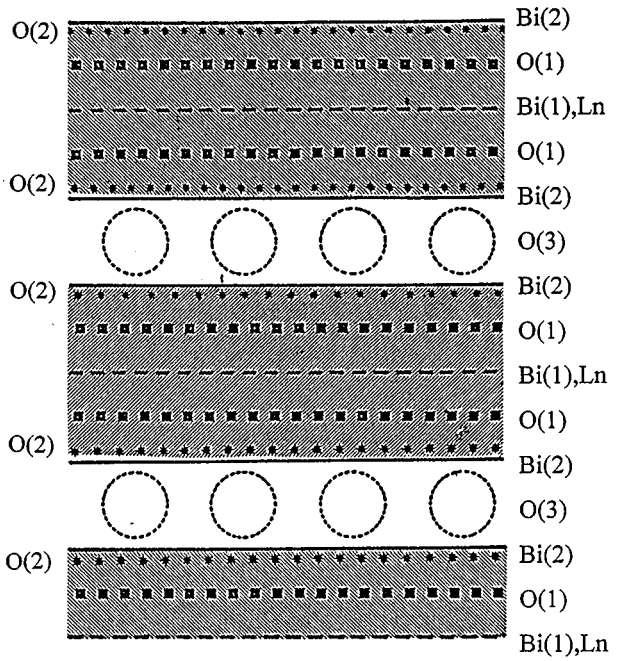

FIG. 7. $Bi_{0.775}Ln_{0.225}O_{1.5}$ layer type structure.

decrease of the conductivity level of the studied materials from La to Dy sample.

The activation energies are related to the facility of slab → interslab motion for $O_{(2)}$ ions, leading to an increase of the number of charge carriers in the conduction space. This justifies the increase of E_a from La to Dy sample resulting from the decrease of $O_{(2)} \rightarrow O_{(3)}$ pathway window radius, directly related to the *a* cell parameter. The facility of $O_{(2)}$ ions extraction closely depends on the cationic order in the mixed layer, thus justifying the two Ln^{3+} radius $-E_a$ dependence domains.

A doubt remains concerning the Eu-containing material: the results corresponding to the lattice parameters (*a* and *c* ambient values and thermal expansion coefficients) and the isothermal conductivity show that this sample belongs to the first set (*Ln* = La, Pr, Nd, Sm), whereas the results corresponding to the Rietveld refinements and to the activation energies, lead to its identification as part of the second set (*Ln* = Gd, Tb, Dy). It would be possible in fact that this material exhibits either the first or the second type of cationic order in the mixed layer depending on the final thermal treatment of the material.

An investigation of these samples by electron microscopy has been undertaken, in order to confirm the different possibility of Bi/*Ln* order within the mixed cationic layers of the slabs, and also to identify the supercell dimensions. Until now, data obtained on La- and Dy-containing samples unambiguously prove the existence of these superstructures; this work is currently under progress and will appear in a further publication.

CONCLUSION

Investigations of $Bi_{0.775}Ln_{0.225}O_{1.5}$, with *Ln* = La, Pr, Nd, Sm, Eu, Gd, Tb, Dy, presenting a layer-like structure with the Bi–Sr–O rhombohedral type, have brought interesting informations on this family of materials: two different subfamilies can be identified, one from La to Sm, and another one from Gd to Dy, with the Eu containing member as the intermediary link. This was established from evolutions versus Ln^{3+} radius of room temperature lattice parameters, cell dimension thermal expansion coefficients, and layer structural characteristics (multisheet slab thickness and interslab gap dimensions). Both families adopt the β_2 low-temperature crystallographic form, their difference being attributed to a specific cation ordering within the mixed layer of the cationic slab. The decrease of the conductivity performances of the phases from La to Dy sample can be explained and correlated to the evolution of the structural characteristics.

TABLE 5
Anisotropic ($\beta \times 10^4$), Equivalent (B_{eq}) Cationic, and Isotropic (B_{iso}) Anionic Thermal Parameters for $Bi_{0.775}Ln_{0.225}O_{1.5}$ ($\beta_{11} = \beta_{22} = 2\beta_{12}$; $\beta_{13} = \beta_{23} = 0$)

	$Bi_{(1)}$, *Ln*			$Bi_{(2)}$			$O_{(1)}$	$O_{(2)}$, $O_{(3)}$
Ln	β_{11}	β_{33}	B_{iso}	β_{11}	β_{33}	B_{iso}	B_{iso}	B_{iso}
La	147(11)	11.0(3)	1.6(1)	303(8)	4.5(1)	1.4(1)	3.3(7)	2.4(7)
Pr	33(12)	5.9(3)	0.7(1)	125(7)	1.3(1)	0.5(1)	0.8(5)	1.3(7)
Nd	122(13)	11.4(3)	1.5(1)	256(8)	7.6(1)	1.6(1)	5.0(8)	2.1(7)
Sm	79(22)	6.0(5)	0.8(1)	181(13)	3.3(2)	0.9(1)	1.9(9)	1(1)
Eu	348(15)	7.9(4)	1.9(1)	353(9)	5.0(2)	1.6(1)	4.6(8)	4.1(9)
Gd	259(11)	8.9(2)	1.7(1)	342(6)	5.7(1)	1.6(1)	3.3(5)	1.8(5)
Tb	347(14)	4.8(3)	1.6(1)	399(9)	3.3(2)	1.6(1)	4.4(8)	3.8(8)
Dy	337(18)	6.9(4)	1.7(1)	403(11)	4.0(2)	1.7(1)	3.0(8)	2.6(9)

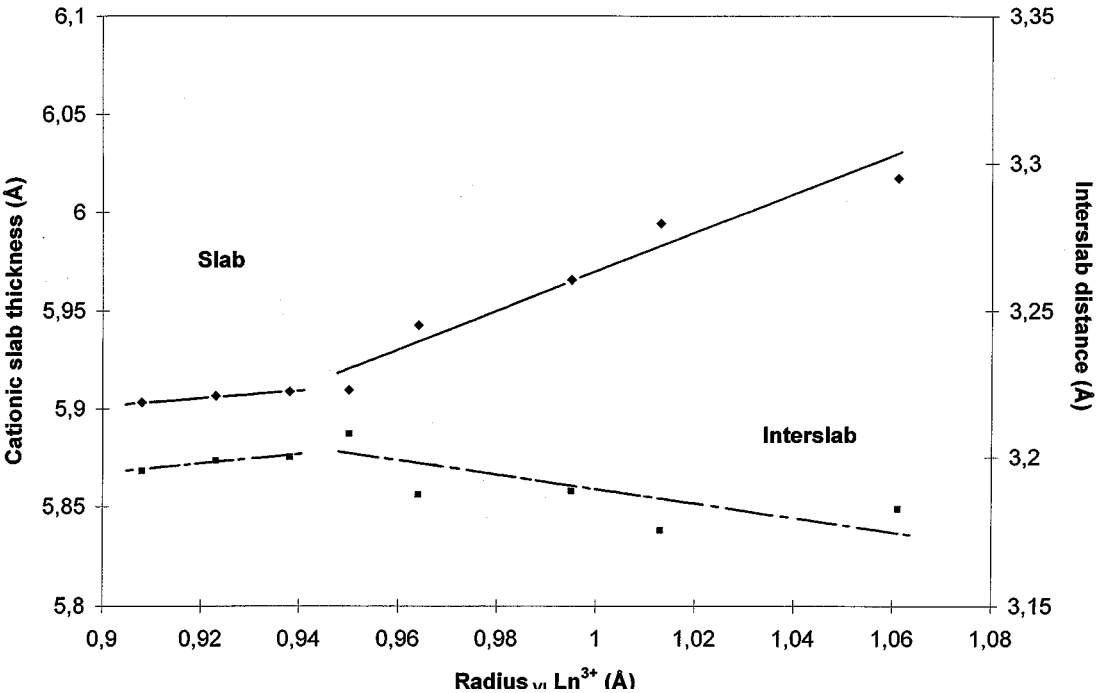

FIG. 8. Evolution of cationic slab thickness and interslab gap size versus Ln_{VI}^{3+} radius.

REFERENCES

1. P. Conflant, J. C. Boivin, and D. Thomas, *J. Solid State Chem.* **18,** 133 (1976).
2. R. Guillermo, P. Conflant, J. C. Boivin, and D. Thomas, *Rev. Chim. Minér.* **15,** 153 (1978).
3. P. Conflant, J. C. Boivin, G. Nowogrocki, and D. Thomas, *Solid State Ion.* **9/10,** 925 (1983).
4. A. Watanabe and T. Kikuchi, *Solid State Ion.* **21,** 287 (1986).
5. A. Watanabe, *Solid State Ion.* **34,** 35 (1989).
6. P. Conflant, C. Follet-Houttemane, and M. Drache, *J. Mater. Chem.* **1,** 649 (1991).
7. A. Watanabe, M. Drache, J. P. Wignacourt, P. Conflant, and J. C. Boivin, *Solid State Ion.* **67,** 25 (1993).
8. A. El Harrak, P. Conflant, M. Drache, and J. C. Boivin, *J. Chim. Phys.* **88,** 2281 (1991).
9. M. Drache, P. Conflant, and J. C. Boivin, *Solid State Ion.* **57,** 245 (1992).
10. P. Conflant, J. C. Boivin, and D. Thomas, *J. Solid State Chem.* **35,** 192 (1980).
11. P. Conflant, Thesis, University of Lille, 1985.
12. M. Drache, J. P. Wignacourt, and P. Conflant, *Solid State Ion.* **86–88** 289 (1996).
13. D. Mercurio, M. El Farissi, J. C. Champarneaud-Mesjard, B. Frit, and P. Conflant, *J. Solid State Chem.* **80,** 133 (1989).
14. D. Mercurio, J. C. Champarneaud-Mesjard, B. Frit, P. Conflant, J. C. Boivin, and J. B. Vogt, *J. Solid State Chem.* **112,** 1 (1994).
15. S. K. Blower and C. Greaves, *Mater. Res. Bull.* **23,** 765 (1988).
16. R. J. D. Tilley, *J. Solid State Chem.* **41,** 233 (1982).
17. R. L. Withers and H. Rossell, *J. Solid State Chem.* **118,** 66 (1995).
18. H. M. Rietveld, *Acta Crystallogr.* **22,** 151 (1967).
19. H. M. Rietveld, *J. Appl. Crystallogr.* **2,** 65 (1969).
20. J. Rodriguez-Carvajal, M. T. Fernandez-Diaz, and J. L. Martinez, *J. Phys. Condensed Mater.* **3,** 3215 (1991).
21. D. B. Wiles and R. A. Young, *J. Appl. Crystallogr.* **14,** 149 (1981).
22. D. B. Wiles and R. A. Young, *J. Appl. Crystallogr* **15,** 430 (1982).
23. C. Caglioti, A. Paoletti, and E P. Ricci, *Nucl. Instrum. Methods* **3,** 223 (1958).
24. R. D. Shannon and C. T. Prewitt, *Acta Crystallogr. B* **26,** 1046 (1970).
25. R. D. Shannon, *Acta Crystallogr. A* **32,** 751 (1976).